

A Modular Double Electrode Flow Cell with Exchangeable Generator and Detector Electrodes

Frederik J. Stender,^[a] Keisuke Obata,^[b] Max Baumung,^[a, c] Fatwa F. Abdi,^[b] and Marcel Risch^{*[a, c]}

Generator-collector experiments offer insights into the mechanisms of electrochemical reactions by correlating the product and generator currents. Most commonly, these experiments are performed using commercially-available rotating ring-disk electrodes (RRDE). We developed a modular double electrode flow cell (DEFC) with exchangeable generator and detector electrodes where the electrode width equals the channel width. As a test case, we considered the ferri-/ferrocyanide redox couple in experiments, analytical calculations and multiphysics simulations. Wall effects reduce the current density by less than 10% in our geometry for the investigated conditions and the analytical solution for the limiting current at the generator

electrode applies to widths up to 5 mm. The collection efficiency for all investigated electrode widths is close to the expected 35.4% above a flow rate of 1.0 (mL/min)^{1/3} but only independent of the flow rate for electrodes with width 5 mm and larger. Kinetic constants of 1.3–1.9·10⁻³ cm/s are obtained from Koutecký-Levich analysis and 21.0–5.0·10⁻³ cm/s from Nicholson analysis for the DEFC, which falls within the range reported previously. We conclude that our DEFC with exchangeable electrodes is an attractive alternative to commercial RRDEs which offers the flexibility to optimize both the generator and collector materials for the desired reaction.

Introduction

Mechanisms of electrochemical reactions can be studied with generator-collector experiments by correlating the product and generator currents.^[1,2] A common method is based on driving a redox reaction on the generator electrode and detection of the reverse reaction on the collector electrode,^[3–8] which works for fast redox couples^[1,9] and detection of catalytic products.^[10–13] Electrochemical detection has several requirements. First, the reaction needs to be chemically reversible in order to be detected and the product has to be chemically stable until reaching the detection electrode. Second, possible side products or (semi)stable intermediate products must have a sufficiently different redox potential from the species in

question to separate them.^[5] Third, the transport of the product towards the collector should be well-defined.

Generator-collector experiments are most commonly performed using rotating ring-disk electrodes (RRDE; Figure S1),^[11–13] which are commercially available from several manufacturers. In this kind of setup, a rotated disk is the generator electrode. The rotation induces a laminar flow of the electrolyte on the disk. The collector electrode is a concentric ring electrode, which is separated by a small isolating gap from the disk. In most RRDE-setups, the disk is exchangeable, in contrast to the ring.

An interesting but less popular setup for generator-collector experiments is the double electrode flow cell (DEFC),^[1,14–17] where the generator and collector electrodes are embedded in a flow channel. Here, we only consider rectangular macrofluidic channels (Figure 1) but other geometries, e.g., tubes, are also possible.^[10,13,18] Mass transport in DEFCs of various geometries

[a] F. J. Stender, M. Baumung, Dr. M. Risch
Institut für Materiaphysik
Georg-August-Universität Göttingen
Friedrich-Hund-Platz 1, 37085 Göttingen (Germany)
E-mail: mrisch@material.physik.uni-goettingen.de

[b] Dr. K. Obata, Dr. F. F. Abdi
Institut für Solare Brennstoffe
Helmholtz-Zentrum Berlin für Materialien und Energie GmbH
Hahn-Meitner-Platz 1, 14109 Berlin (Germany)

[c] M. Baumung, Dr. M. Risch
Nachwuchsgruppe Gestaltung des Sauerstoffentwicklungsmechanismus
Helmholtz-Zentrum Berlin für Materialien und Energie GmbH
Hahn-Meitner-Platz 1, 14109 Berlin (Germany)
E-mail: marcel.risch@helmholtz-berlin.de
Homepage: http://www.helmholtz-berlin.de/forschung/oe/ce/oxygen-evolution/index_en.html

Supporting information for this article is available on the WWW under <https://doi.org/10.1002/celec.202300126>

© 2023 The Authors. ChemElectroChem published by Wiley-VCH GmbH. This is an open access article under the terms of the Creative Commons Attribution License, which permits use, distribution and reproduction in any medium, provided the original work is properly cited.

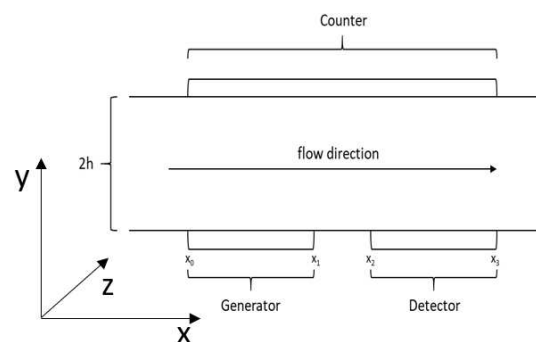


Figure 1. Schematic drawing of the flow cell. x_0 represents the start of the generator electrode and x_1 the end. x_2 represents the start of the collector electrode and x_3 the end. The gap between both electrodes has the size $x_2 - x_1$.

and dimensions has been well investigated experimentally, theoretically and by simulations for both coupled operation (as in this work) and sequential operation (leading to array measurements).^[19–26] In well-constructed setups, a laminar flow transports the products from the generator to the collector electrode. Flow cells are also commercially available from several sources but only a single DEFC with two non-exchangeable disk electrodes is commercially available (for use in liquid chromatography). Self-made DEFCs offer the possibility to optimize the geometry for the target application and to make both the generator and collector electrodes exchangeable to study different reactions. Moreover, it is easy to integrate flow cells with additional analysis tools^[27] such as UV-vis,^[28,29] X-ray^[30,31] or mass spectrometers^[2,32] to gain more comprehensive insight into the electrochemical reactions at the generator electrode.

Here, we discuss a self-made DEFC as an electroanalytic tool for generator-collector experiments and compare a commercial RRDE system,^[10,33–35] with which most electrochemists are more familiar. Our DEFC was designed in such a way that rectangular electrodes of different sizes can be easily clamped into and removed from the channel for post mortem analysis. The well-known ferro-/ferricyanide redox couple^[36] was used as the analyte to compare both systems in terms of transport limiting currents, collection efficiency and kinetics. Three-dimensional simulations were conducted for the DEFC to gain further insight into the flow behavior of the electrolytes to elucidate possible boundary effects at the channel wall. The limiting generator current and collection efficiency of our DEFC design can be described analytically for electrode widths of 5 mm. The obtained kinetic constants are comparable to an RRDE and fall in the range of reported values.

Results and Discussion

Construction of the DEFC

The experimental setup of the developed DEFC implements a four-electrode setup along a channel with two 5 mm long working electrodes on the floor of the channel separated by a 1 mm gap. The upstream working electrode serves as the generator electrode and the downstream working electrode as the collector electrode. A 11 mm long counter electrode is situated directly above the two working electrodes realizing a parallel plate configuration (Figure 1). The geometrical parameters of our flow cell are summarized in Table 1. The working electrodes are clamped into a modular body and tightened with PTFE tape and parafilm as gaskets. The clamping allows easy removal of the electrodes for post-mortem investigations, and a wide range of differently prepared electrodes can be used without modification of the cell body. As the electrodes are clamped by the backside onto the channel, their width matches that of the channel ($d=w$), which is a common geometry for microchannel electrodes and arrays.^[21,24–26] In this respect, our design differs from previous macro-sized DEFCs where a smaller electrode is placed in the middle of a larger

Table 1. Geometric parameters of the DEFC.

Description	Variable	Value
Length of generator electrode	$x_1 - x_2 = l_{gen}$	5 mm
Width of generator electrode	$z_1 - z_0 = w$	2.0, 5.0*, 7.5 mm
Gap	$x_0 - x_1 = g$	1 mm
Length of collector electrode	$x_3 - x_2 = l_{col}$	5 mm
Width of collector electrode	$z_3 - z_2$	2.0, 5.0*, 7.5 mm
Channel height	$2h$	1 mm

*Used channel width for the experiments if not noted differently.

channel and the implications of this geometry was not thoroughly addressed in literature for micro-sized electrodes. Channel widths of 2.0 mm, 5.0 mm and 7.5 mm were selected for experiments, which results in different center velocities, v_o , for each channel width at constant volume flow velocity, V_f . Furthermore, the physical size of the electrode remained identical so that a smaller channel width results in a smaller utilized fraction of the electrode, i.e., active area. The reference electrode was placed upstream and close to the generator electrode to avoid issues with product interference (if gas would be produced) and to accurately reflect the potential at the generator electrode. Moreover, the geometry of parallel working and counter electrodes was chosen to ensure homogeneous equipotential surfaces parallel to the electrode surfaces, which minimize the error of the potential measurement and ensure better potentiostat stability.

Analytical solutions for the constructed DEFC

The transport of the analytes within the cell needs to be understood to predict and understand the measured currents. The DEFC is a well-defined hydrodynamic system, in which diffusion as well as convection determine the transport of the analytes towards the electrodes.

The faradaic current of a fast redox reaction (i.e., without coupled kinetics; eq. 1)



is given by eq. 2

$$i = nF \int J dS \quad (2)$$

where i is the current, n is the number of electrons involved in the redox-reaction, F is the Faraday constant, S is the area and J is the flux of the redox couple normal to the electrode surface. Laminar flow is assumed in the theoretical treatment in textbooks,^[1,37,38] i.e. the Reynolds number should not exceed 2000 to avoid turbulent flow.^[35] It is expressed as (eq. 3):

$$Re_{DEFC} = \frac{2hv_0}{\nu} = \frac{3V_f}{2\nu d'} \quad (3)$$

where h is the half-height of the channel, v_0 is the velocity at the center of the channel ($y=h, z=d/2$), ν is the kinematic viscosity of the solution, d is the width of the channel and V_f is the volume flow rate.

The convection-diffusion equation describes the concentration change of species A (eq. 1) due to convection and diffusion. It is given by eq. 4

$$\frac{\partial[A]}{\partial t} = D_A \nabla^2[A] - \left(v_x \frac{\partial[A]}{\partial x} + v_y \frac{\partial[A]}{\partial y} + v_z \frac{\partial[A]}{\partial z} \right), \quad (4)$$

where D_A is the diffusion constant of species A, $[A]$ is the concentration, $v_{x,y,z}$ are the velocity profiles in the x, y, z directions as defined in Figure 1. Under steady state conditions, the time dependency is removed as there is no change in the velocity and concentration profiles over time.

The diffusion in x, z -direction can be neglected for the DEFC due to fast convection in comparison to diffusion.^[35,37,39] Additionally, it is assumed that the velocity in all other directions is negligible ($v_y=v_z=0$) for laminar flow in x direction. This reduces eq. 4 to eq. 5

$$0 = D_A \frac{\partial^2[A]}{\partial y^2} - v_x \frac{\partial[A]}{\partial x}. \quad (5)$$

Under the assumption of $d \ll 2h$ and using the L ev eque approximation, the velocity profile close to the electrode can be linear approximated (eq. 6)^[1,35,40,41]

$$v_x = v_0 \left(\frac{h^2 - (y-h)^2}{h^2} \right) \approx \frac{2v_0 y}{h} = \frac{3V_f y}{2h^2 d} \quad (6)$$

for $y=0$ with

$$V_f = \frac{4}{3} v_0 h d. \quad (7)$$

Eq. 6 is plotted in Figure 2a for illustration. The solution of eqs. 2 and 5 using the approximation in eq. 6 results in eq. 8 that describes the limiting current of a first-order reaction^[35]

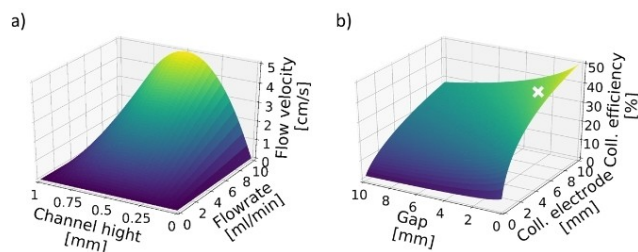


Figure 2. a) Analytically calculated flow field distribution over the height of the channel for different flow rates. b) Expected collection efficiency as function of the collection electrode and gap size according to analytical calculations as detailed in the text (Eq. 10). The white cross marks the collection efficiency of the experimentally used flow cell in this study, i.e., 35.4%. In both cases, the total channel height was 1 mm, the width was 5 mm and the length of the generator electrode was 5 mm.

$$|i_{\text{lim,DEFC}}| = \alpha n F w D^{\frac{2}{3}} \left(\frac{V_f}{h^2 d} \right)^{\frac{1}{3}} \beta^{\frac{2}{3}} c_{\infty}, \quad (8)$$

where w is the width of the active electrode area, c_{∞} is the bulk concentration, l is the length of the electrode and α is a prefactor that comes from the geometry and flow velocity distribution and has the value $\alpha=0.925$ when h is the half height of the channel (as in this work). Note that a prefactor of $\alpha=1.467$ can be found in literature^[39] when h is the height of the channel. The calculation assumes that the electrode is placed in the middle of the channel and sufficiently away from the walls, to avoid flow disturbances. The corresponding diffusion layer thickness at the electrode can be expressed as eq. 9^[39]

$$z_D = \beta h \left(\frac{x D d}{h V_f} \right)^{1/3}. \quad (9)$$

Where the prefactor β has the value 1.62162.

The theoretical collection efficiency of a DEFC, N_{DEFC} , for electrochemically reversible reactions can be analytically calculated as (eq. 10)^[10]

$$N_{\text{DEFC}} = 1 + \lambda^2 [1 - F(\theta)] - (1 + \theta + \lambda)^2 \cdot \left[1 - F\left(\frac{\theta}{\lambda} (1 + \theta + \lambda) \right) \right] - F\left(\frac{\theta}{\lambda} \right), \quad (10)$$

With

$$\theta = \frac{x_2 - x_1}{x_1}$$

$$\lambda = \frac{x_3 - x_2}{x_1}$$

and the function (eq. 11)

$$F(\theta) = \frac{\sqrt{3}}{4\pi} \ln \left[\frac{(1 + \theta^2)^3}{1 + \theta} \right] + \frac{3}{2\pi} \tan^{-1} \left[\frac{2\theta^2 - 1}{\sqrt{3}} \right] + \frac{1}{4}, \quad (11)$$

where x_1 is the length of the generator electrode, x_2 is the sum of the length of the generator electrode and the gap length and x_3 is the sum of the length of the generator electrode, the gap length and the length of the collection electrode (Figure 1). Compton and Stearn^[42] showed experimentally (using the ferri-/ferrocyanide redox couple) and by simulations that eq.(10) underestimates the collection efficiency of macro-sized DEFCs for flow rates below about 6 mL/min, which is in the middle of the range investigated here (1–10 mL/min; more discussion below). The L ev eque approximation (eq. 6) overestimates v_x resulting in a lower prediction of product detection when using Eq. (10).

The analytically calculated collection efficiencies for varying gap lengths (effects parameter x_2, x_3 , between 0.1 and 5 mm)

and lengths of the detection electrode (effects parameter x_3 , from 0.1 to 10 mm) are plotted in Figure 2b. The resulting collection efficiencies range from 2.3% (5 mm gap, 0.1 mm detection electrode) to 50% (0.1 mm gap, 10 mm detection electrode).

The analytic solutions are valid for the investigated experimental parameters if 3D effects can be neglected. For flow rates of 0.5 to 8 mL/min, the Reynolds number of our DEFC was calculated in the range of $Re_{DEFC}=2.5$ to 40 ($\nu = 0.01004 \text{ cm}^2/\text{s}$ at 20°C) using eq. (3). The low Reynolds number ($< < 2000$) suggests that our DEFC has a laminar flow in the used range of flow rates, which allows a controlled mass transport to and from the working electrodes. The ratio between the Peclet number ($Pe = V_f / (d^* D)$) and a dimensionless working electrode length $L = l / (2h)$ was identified as an indicator for the validity of the Levich equation (eq. 8) for microfluidic channels.^[43] For the here presented cell geometry and flow rates, a high Pe/L (Table S1) was calculated suggesting that the Levich equation should be valid also for our macro-sized channel. The high ratio also suggests, that only a small part of the electrolyte close to the electrode surface affects the electrochemical reaction.^[43] However, this estimation is a result of 2D calculations and may not consider 3D wall effects that we studied by simulations.

Numerical simulations of the DEFC

Multiphysics finite-element simulations were performed to initially check the applicability of the analytical calculations above, to gain further insight into the mass transport in the DEFC and to elucidate possible wall effects. Previously, simulations were used to understand mass transport in macrofluidic cells of various configurations^[22,44,45] and microfluidic cells, particularly those with same width of the electrode and channel.^[23–26] Identical parameters were used in the analytical calculations and our simulations (Table 2). The simulations do not require some of the assumptions made in the analytical calculations as discussed below regarding laminar flow, the velocity profiles (i.e., L ev eque approximation) as well as the current and product distributions.

The low Reynolds number predicted laminar flow. Yet, the liquid inlet may cause a disturbance to the laminar flow. Simulations of our cell geometry show that the disturbance of the inlet only affects regions within ~ 5 mm from the inlet (Figure S2). As the inlet is separated by 35 mm from the generator electrode, we conclude that the flow is uniform and

laminar over the 5 mm length (x coordinate in Figure 1) of the generator and also collector electrode.

The 2D analytical calculations assume uniform velocity over the full width of the channel (z direction in Figure 1) but the velocity was reduced in the simulations near the walls ($z=0.0$ and $z=5.0$ mm). This is shown in Figure 3a for half the channel height (y coordinate) and half the electrode width (z coordinate). The simulation is symmetric relative to these half points. For the simulation of the $w=2.0$ (Figure S3a and 4), $w=5.0$ mm (Figure 3a and 4) and $w=7.5$ mm (Figure S4) electrodes, the wall affects only the leftmost 0.2 and 0.5 mm (dashed white lines), i.e., about 20% of the electrode width. The assumption of a uniform velocity in the direction of the channel width (z coordinate) is still reasonably fulfilled for these electrodes and potentially larger electrodes, because the changes in the velocity close to the electrode surface are small.

The current density distribution over the generator electrode resulting from the non-uniform velocity profile is shown in Figure 3b, where again the symmetric half point is shown for the electrode width (z dimension) and length (x dimension / flow direction). The current density decreases from $-1.2 \text{ mA}/\text{cm}^2$ at the electrode edge toward the inlet to $-0.15 \text{ mA}/\text{cm}^2$ within about 2 mm in flow direction, where the largest decrease of the current occurs in the first 0.5 mm. The current density is reduced toward the wall ($z=5.0$ mm) but since the reduction is strongest in the first 10% in flow direction, the walls likely have only a minor effect on the current density when the electrode is long and wide as compared to the region affected by the wall as in our design. The simulations of the DEFC with $w=2.0$ mm and $w=7.5$ mm (Figure S3c,e and S4–6) were similar to those of with $w=5.0$ mm (Figure 3b and S4–6).

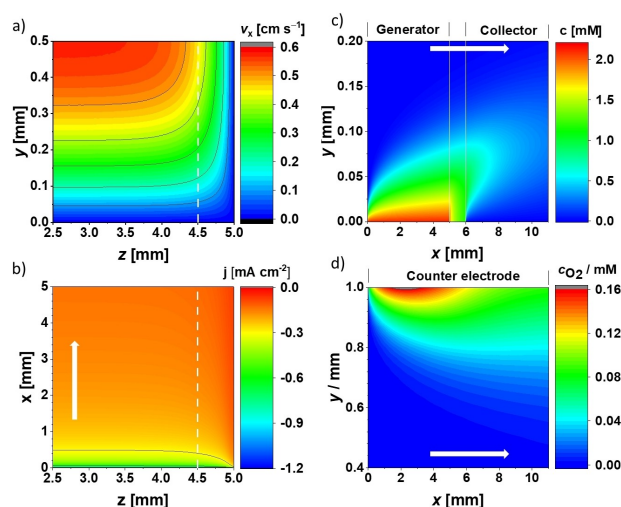


Figure 3. Numerical simulations of the DEFC ($w = 5$ mm). a) Flow velocity field at a flow rate of 1 mL/min along the width (z) and the height of the channel (y) due to the symmetry of the system only the half width and height are displayed. b) Local current density on the generator at 1 mL/min. The symmetry boundary is located at $z = 2.5$ mm. c) Concentration distribution of $\text{Fe}(\text{CN})_6^{4-}$ in the middle of the channel ($z = 2.5$ mm) at 1 mL/min d) Concentration distribution of dissolved O_2 at 1 mL/min at the middle ($z = 2.5$ mm) of channel. The white arrows symbolize the flow direction (x-direction). The vertical line in panel a and b indicates the region with the most pronounced changes due to the wall.

Table 2. Parameters of analytical calculations and simulations.

Description	Variable	Value
Bulk concentration $[\text{Fe}(\text{CN})_6]^{3-}$	$c_{0, [\text{Fe}(\text{CN})_6]^{3-}}$	2 mM
Diffusion coefficient $[\text{Fe}(\text{CN})_6]^{3-}$	$D_{[\text{Fe}(\text{CN})_6]^{3-}}$	$7.31 \cdot 10^{-6} \text{ cm}^2/\text{s}$
Diffusion coefficient $[\text{Fe}(\text{CN})_6]^{4-}$	$D_{[\text{Fe}(\text{CN})_6]^{4-}}$	$6.71 \cdot 10^{-6} \text{ cm}^2/\text{s}$
Diffusion coefficient O_2	D_{O_2}	$2.40 \cdot 10^{-5} \text{ cm}^2/\text{s}$
Kinematic viscosity of water	ν	$0.010023 \text{ cm}^2/\text{s}$

The product distribution at both working electrodes (Figure 3c) was subsequently simulated. At the generator electrode, ferricyanide ($\text{Fe}^{\text{III}}[\text{CN}]_6^{3-}$) is reduced to ferrocyanide ($\text{Fe}^{\text{II}}[\text{CN}]_6^{4-}$) and the reverse reaction occurs at the collector electrode. The concentration of ferrocyanide is highest near the generator electrode ($y=0.0$ mm) and decays to the bulk value of zero within a height of 0.15 mm above the electrode (y dimension). In the direction of the flow (x dimension), the concentration increased parabolic in height (y). The ferrocyanide concentration was about 1 mM in the gap to a height of 0.07 mm and then quickly decayed to zero. The concentration of ferrocyanide also vanished near the collector electrode as expected. The contour line of 0.5 mM (light teal) illustrates that the concentration decrease was parabolic in height.

In the next step, we simulated the product distribution above the counter electrode located at $y=1.0$ mm (Figure 3d). An oxidation reaction must occur for charge conservation at the counter electrode because a reduction reaction occurs at the generator electrode and the collection efficiency of the collector electrode is $<100\%$. Since ferricyanide cannot be oxidized further, the most likely component in the electrolyte to oxidize is water by the oxygen evolution reaction ($2\text{H}_2\text{O} \rightarrow 4\text{H}^+ + 4\text{e}^- + \text{O}_2$). For low and intermediate O_2 concentrations (<0.04 mM), the distribution was again nearly parabolic in height (y dimension) as expected from the analytic solution of the diffusion layer thickness (eq. 9). The simulations reveal that the highest concentrations of 0.12 to 0.16 mM and therefore also the highest current density were observed above the generator electrode ($0 < x < 5$ mm) with a semicircular distribution. Overall, the simulations of the product distributions show that the products of the working and counter electrodes do not mix over the generator and collector electrodes for the chosen channel height of 1 mm and the investigated flow rates.

Simulation of wall and edge effects

The influence of the wall versus the electrode edge was further investigated in more detail by simulating a more conventional cell configuration with a 2 mm wide electrode in the center of the channel having widths 5 mm and comparison new configuration having equal width of electrode and channel of 2 mm (Figure 4, Figure S4–6). For the latter case of identical electrode and channel, the concentration of ferricyanide over the electrodes decreases at fixed height (y -coordinate) from the electrode surface due to a lower flow velocity close to the channel wall ($z=2.0$ mm). As mentioned above for the case $w=d=5$ mm, this leads to a decrease in current density toward the channel wall, which is also the electrode edge (Figure S3c). In case of using an electrode smaller than the channel width ($w=2$ mm, $d=5$ mm) the concentration of unconsumed reaction educts increased at the electrode edges at fixed height (y -coordinate), as a result of diffusion from the bulk of the electrolyte towards the electrode edges. This led to a larger current density at the edge (Figure 4d). The current density was lower for this case as compared to the configuration with equal electrode and channel width ($w=d=2$ mm) due to the lower

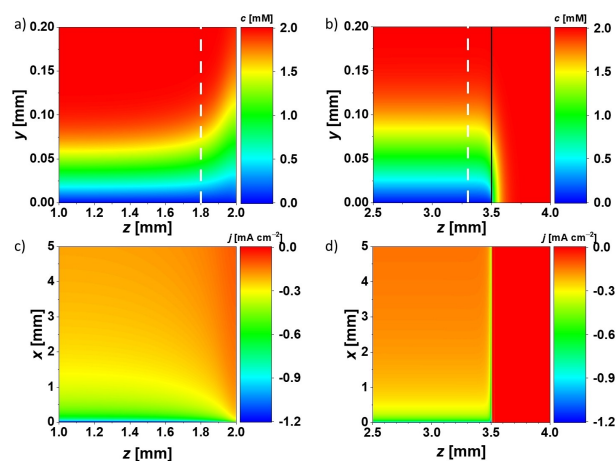


Figure 4. Investigations of the effect of the wall on the generator electrode by numerical simulations at a flow rate of 1 mL/min. (a,b) concentration profile of $\text{Fe}(\text{CN})_6^{3-}$ in the middle of the electrode ($z=2.5$ mm) and (c,d) current distribution on the electrode of a channel with (a,c) $w=d=2$ and (b,d) $w=2$, $d=5$. The white dashed line indicates the region with the most pronounced changes due to the wall. The black line indicates the edge of the electrode in the $w=2$, $d=5$ configuration.

flow velocity, v_w , in the larger channel at the same volume flow rate, V_f (Eq. 7; Figure S4). The simulations of the concentrations of the ferrocyanide at the collector electrode (Figure S3f, g) show a similar effect regarding the wall as compared to the generator electrode.

The comparison of 2D and 3D simulations (Figure S7) give additional insight into the wall effects due to the fact, that 2D simulations assume uniform velocity over the full width of the electrode and no diffusion in flow direction (x coordinate) and above the electrode (y coordinate), while the 3D simulations take into account the slower flow at the walls as well as diffusion from the bulk electrolyte (along the z coordinate) to an electrode smaller than the channel width. When the electrode width equals that of the channel (configuration $w=d=2$ mm), then the 2D and 3D simulations had nearly the same current densities of the generator and collector electrodes (Figure S7a). However, in the case of a narrow electrode in a wider channel ($w=2$ mm, $d=5$ mm), the generator current of the 3D simulation was higher than that of the 2D simulations (Figure S7b) due to diffusion from the bulk electrolyte toward the edge of the electrode. This indicates that edge effects should be considered for the more commonly investigated macroscopic case where the electrode is narrower than the channel, e.g., refs. [19, 20, 46].

Wall and edge effects manifested as a reduction of the current density at the wall/edge (z coordinate) and became more pronounced in flow direction (x coordinate) on the electrode (Figure S6). The magnitude of the changes at the wall/edge increased with decreasing channel size and increasing volume flow rate as also seen in the concentration and flow velocity (Figure S4–6). We quantified the observed changes by taking the average along the x coordinate in the middle of the electrode as an estimate of an infinite electrode without wall/edge effects and the average over the area of the electrode. For

$w=d=7.5$ mm and 1 mL/min with the smallest wall effect, the wall reduces the average current density by 4%, while for $w=d=2$ mm and 10 mL/min with the largest wall effect, the wall reduces the average current density by 10%. Therefore, the simulations suggest that wall effects are small for our experimentally realized case of equal electrode and channel width and flow rates. We rationalize it by the absence of eddy diffusion from the bulk electrolyte due to the wall in contrast to the case $w=2$ mm, $d=5$ mm. Thus, we focus on the configuration with equal electrode and channel width in our experimental case study, which we expect to agree with the analytic solutions to within 10% or better.

Experimental case study

We assembled the DEFC with generator ($w=d=5.0$ mm) and collector electrodes made from Pt to test its response with ferricyanide in a potassium chloride supporting electrolyte (Figure 5). Additional measurements of the DEFC with widths $w=(d=)$ 2.0 and 7.5 mm are shown in Figure S9. We experimentally investigated flow rates between 0.5 and 6 mL/min, where the lower flow rate was chosen for the desired fast detection of the product and the upper flow rate was determined by the specifications of the used syringe pump. The DEFC measurements are precisely reproduced on different laboratory days (Figure S10). All measurements show exponential currents at the generator and collector electrodes with opposite signs between 0.3 and 0.1 V vs. a saturated calomel electrode (SCE), where mainly the kinetics of the ferri-/ferrocyanide redox limit the current. The current was constant below 0.1 V vs. SCE due to limited mass transport of the ferricyanide analyte, akin to RRDE measurements (Figure S8). The half-wave potentials at both the DEFC (and RRDE, Figure 5, Figure S8 and 9) decrease slightly by ~ 10 mV with increasing flow rate and rotation speed, which suggests partial limitation by mass transport at the investigated low flow rates and rotation speeds. The DEFC gives a value of 0.2 V vs SCE, which was similar to the literature value^[47] of 0.19 V.

In order to account for effects not modeled in the analytical solution or simulations, we compare the shape of the CV trace

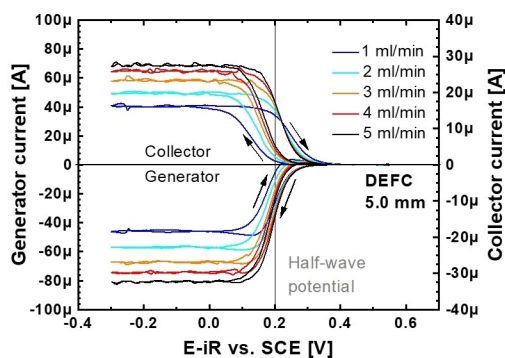


Figure 5. Cyclic voltammograms of the DEFC with $w=5.0$ mm with flow rates between 1 to 5 mL/min. The grey lines indicate the half-wave potential and arrows the scan direction.

to that obtained by an RRDE as well as the values of the limiting and kinetic currents. A closer inspection of the data shows that the DEFC produced slightly noisier data and exhibits stronger hysteresis as compared to the RRDE (Figure 5 and Figure S9 vs. S8). The source of the noise are small fluctuations of the flow velocity due to the used syringe pump and slipping of the syringe plunger. The noise is visible but minor and does not influence the analyses below, which are based on average currents to reject the noise. The hysteresis was more pronounced for slower flow rates and smaller electrode width (Figure 5, Figure S9). Its presence may seem surprising as the generator and collector electrodes are separated by 1 mm in both systems, yet the relevant flow velocity differs among the DEFC and RRDE so that the time of travel is longer for a DEFC at a comparable limiting current as can be seen at the velocity distribution close to the electrode surface (Figure S12). Furthermore, the DEFC electrodes are longer in flow direction and have a non-uniform current distribution (Figure 3b). Therefore, the hysteresis is a transport related effect that can be avoided by increasing the flow velocity. The hysteresis also did not affect the limiting current at the working electrodes and the corresponding collection efficiency that are discussed in detail below. We further analyze the data to obtain the limiting current of the generator and collector electrodes as well as the resulting collection efficiency for comparison with the analytic solution and simulations presented above. Finally, the kinetic constant is obtained and discussed.

Limiting current of the generator electrode

The measured limiting current of the generator electrodes for the DEFC was compared to the analytical solution as well as simulations, which used typical parameters from literature (Table 2). As expected from eq. 8, the absolute value of the limiting currents of the DEFC (Figure 6) increased with flow velocity, respectively. The limiting generator currents of the DEFC (Figure 6) and RRDE (Figure S8) had similar values for the investigated flow rates and rotation speeds. However, the active

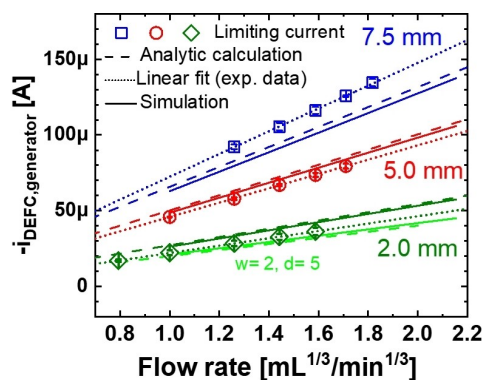


Figure 6. Comparison between analytically calculated, simulated and measured limiting currents for different flow rates and channel widths of the DEFC. The plots are linearized by using the expected exponential function of the flow rate (eq. 8).

area of the electrode was 0.126 cm^2 for the RRDE system but 0.25 cm^2 for the DEFC with $w = 5.0 \text{ mm}$. This indicates, that the diffusion layer must be notably smaller in the RRDE system at these rotation speeds. This is also expected from the theory of the diffusion-layer thickness (eq. 9). A thickness between $20 \mu\text{m}$ (500 rpm) and $45 \mu\text{m}$ (100 rpm) is expected (eq. 9) for the RRDE while $49 \mu\text{m}$ (5 mL/min) to $84 \mu\text{m}$ (1 mL/min) were calculated (eq. S6) at the middle of the 5 mm DEFC.

The slopes in Figure 6 and Figure S8b relate to physical constants of the electrolyte and the geometry of the setup as given by eq. 8 and eq. S22 in the analytical treatment. Table 3 compiles all obtained values. The experimental fit assumed that the fit passes through the origin like the analytical equations. Alternative fits with finite y-axis intercept may be found in Table S2 and Figure S13, Figure S14. As the R^2 values of both models were close to unity, indicating an excellent fit, we discuss the simpler model corresponding to the analytical formulas. For the RRDE, the measured and analytical slopes of the generator electrode agree well (Figure S8b), which indicates that the physical constants can be determined with reasonable accuracy using eq. S22 and serve as a reference for DEFC measurements. For the DEFC, the agreement between the measurement and the analytical calculation depended on the width of the generator electrode, where the narrowest electrode ($w = 2.0 \text{ mm}$) was described best, while the slope was slightly overestimated for $w = 5.0 \text{ mm}$ and clearly underestimated for $w = 7.5 \text{ mm}$ (Figure 6). The simulation of the DEFC with $w = (d =) 2.0 \text{ mm}$, $w = (d =) 5 \text{ mm}$ and $w = (d =) 7.5 \text{ mm}$ resulted in a slope closer to the analytical solution than the measurement. The simulated limiting currents for the $w = 2.0 \text{ mm}$, $d = 5.0 \text{ mm}$ configuration also fit well with the analytical solution. Based on the high values of the Péclet number (Pe ; the ratio of the advective to the diffusive transport rate) of > 3000 for the conditions and geometry used herein ($l/h = 5$; Table S1), we had expected that the analytical Levich equation holds for all investigated geometries and flow velocities.^[43] The deviation between the experiments and both the analytical solution and simulations of the DEFC with $w = (d =) 7.5 \text{ mm}$ requires further investigations that are beyond the scope of this work.

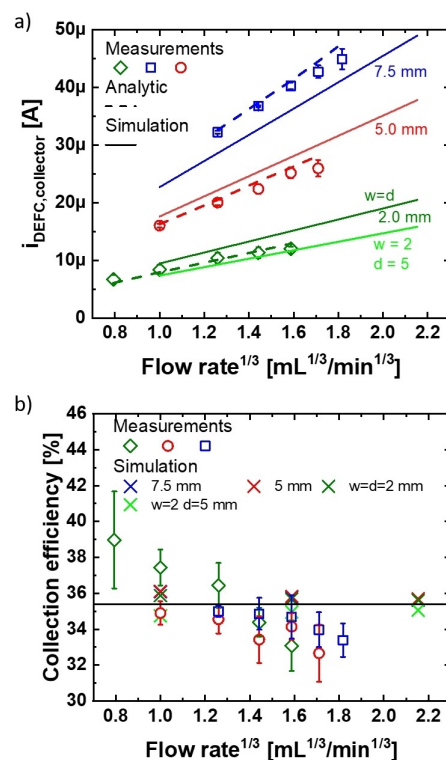


Figure 7. (a) Calculated and measured limiting collection currents and (b) collection efficiencies for the DEFC setup with different channel widths of 2.0, 5.0 and 7.5 mm. Dashed lines indicate the analytical collection efficiency calculated using eq. (10).

Limiting current of the detector electrode and collection efficiency

The measured limiting current of the DEFC collector electrodes and the corresponding collection efficiency were compared to the analytical calculations as well as simulations (Table 4, Figure 7). The collector current was calculated using the analytical collection efficiency and the measured generator currents. This prediction (dashed line) matched the measured collector currents of the DEFC (solid symbols) well (Figure 7a). The simulation of the DEFC with equal electrode and channel width ($w = d$) slightly overestimated the collector current, while the simulation of a narrow electrode in a wide channel ($w = 2 \text{ mm}$, $d = 5 \text{ mm}$) closely matches that of the analytic collector

Table 3. Slopes of current against flow rate obtained from the data in Figure 6.

Device	Analytical* slope	Simulation slope	Experimental fit $y = ax + 0$ slope a	R^2
DEFC, $w = d = 2.0 \text{ mm}$	$-27.3 \mu\text{A min}^{1/3}/\text{cm}$	$-27.0 \mu\text{A min}^{1/3}/\text{cm}$	$22.3(3) \mu\text{A min}^{1/3}/\text{cm}$	0.9994
DEFC, $w = 2.0 \text{ mm}$ $d = 5.0 \text{ mm}$	$-20.1 \mu\text{A min}^{1/3}/\text{cm}$	$-20.8 \mu\text{A min}^{1/3}/\text{cm}$	n/a	n/a
DEFC, $w = d = 5.0 \text{ mm}$	$-50.2 \mu\text{A min}^{1/3}/\text{cm}$	$-49.5 \mu\text{A min}^{1/3}/\text{cm}$	$-46.0(1) \mu\text{A min}^{1/3}/\text{cm}$	1.0000
DEFC, $w = d = 7.5 \text{ mm}$	$-65.8 \mu\text{A min}^{1/3}/\text{cm}$	$-64.6 \mu\text{A min}^{1/3}/\text{cm}$	$-75.7(0) \mu\text{A min}^{1/3}/\text{cm}$	1.0000

Table 4. Collection efficiency of the DEFC.

Device	Analytic N	Simulation N	Experimental fit $y = ax + 0$ N
DEFC, $w = d = 2.0$ mm	0.354	0.354	0.351(9)
DEFC, $w = 2$ mm $d = 5$ mm	0.354	0.353	n/a
DEFC, $w = 5.0$ mm	0.354	0.358(1)	0.337(4)
DEFC, $w = 7.5$ mm	0.354	0.353(1)* 0.357(1)**	0.342(3)

currents. The simulation of the $w = 7.5$ mm channel underestimated the measured collector current.

The collection efficiency was subsequently calculated for DEFC with various electrode widths and compared to the analytical solution and simulations. The DEFC with $w = 5.0$ mm and 7.5 mm showed no apparent trend of the experimental collection efficiency with flow rate and agreed with the analytical solution for all investigated flow rates within two standard deviations where the collection efficiencies of the DEFC with $w = 5.0$ mm are slightly underestimated. Moreover, the faster flow rates may deviate more from the analytical solution as compared to the intermediate ones but further data would be needed to rigorously conclude it. The average experimental collection efficiency of the DEFC with $w = 2.0$ mm decreased with flow rate so that the experimental collection efficiency is larger than the analytical one below 2.7 mL/min (1.4 mL^{1/3} min^{1/3}) and smaller above it (Figure 7b). The changes were not significant within the large experimental standard deviation.

The dependence of the collection efficiency on the flow rate has been discussed previously for macroscopic DEFCs.^[19] The collection efficiency approached 1.0 for very slow flow rates (< 6 μ L/min) due to sufficient time for complete conversion at the detector electrode and the collection efficiency reduced to the value of the analytical solution in eq. (10) at flow rates faster than about 6 mL/min, when the L ev eque approximation applies.^[42] Our simulations do not need this approximation and resulted in collection efficiencies slightly higher than the analytical solution at 4 and 10 mL/min (Figure 7b). We cannot conclusively state whether our data agreed with the previous simulations which would require investigating a wider range of flow rates and better statistics, which is outside the scope of this work.

The collection efficiency was also evaluated by linear regression of the collector current against the generator current (experimental fit in Table 4) for DEFC without dependence on the flow rate, which was in line with the point-by-point evaluation, namely the experimental collection efficiencies of the DEFCs with 7.5 and 5.0 mm were slightly but insignificantly lower than that of the analytical solution. We conclude that the collection efficiency of the investigated electrodes was close to the analytical solutions but slightly lower as the L ev eque approximation is not fully justified as discussed previously.^[42]

Table 5. Kinetic constants in cathodic scan direction obtained from a Kouteck y-Levich plot (K_{KL}^*), including area, A, and y-axis intercept, and the method of Nicholson (K_N^*). Calculation at 0.2 V vs. SCE.

Device	A [cm ²]	y-axis intercept $1/i$ [1/A]	K_{KL}^* [cm/s]	K_N^* [cm/s]
RRDE	0.126(3)	15630(848)	$2.6(3) \cdot 10^{-3}$	$2.1 \cdot 10^{-2}$
DEFC, $w = 2$ mm	0.10(1)	27869(3963)	$1.9(5) \cdot 10^{-3}$	$5.0 \cdot 10^{-3}$
DEFC, $w = 5$ mm	0.25(2)	16259(1478)	$1.3(2) \cdot 10^{-3}$	$2.1 \cdot 10^{-2}$
DEFC, $w = 7.5$ mm	0.375(3)	8930(480)	$1.5(2) \cdot 10^{-3}$	$1.8 \cdot 10^{-2}$

* $k = \frac{i_L}{nFAc}$; Error in concentration, ΔC , very small and not included.

Kinetic studies in a DEFC

The kinetic constants at a potential of 0.2 V vs. SCE close to the half-wave potential were determined for the DEFC using a modified version of the Kouteck y-Levich plot^[48] (Figure S15), which depended weakly on the investigated potential (Figure S16, Tab. S5). The analysis was alternatively performed using the method of Nicholson^[49] where peak-to-peak separations between 62 mV and 76 mV were obtained (Figure S17). No trend could be found regarding the channel width of the DEFC within the fitting error using the Kouteck y-Levich method (Table 5), whereas the Nicholson method showed a decrease of the kinetic constant with increasing electrode width suggesting that narrower electrodes are preferable to minimize the effect of the non-uniform velocity and hence current density distributions on the DEFC on kinetics. Moreover, the kinetic constants obtained by the latter method were up to one order of magnitude higher than the ones calculated by the Kouteck y-Levich method independent of the device. The the Kouteck y-Levich plots were not perfect linear as expected for this method leading to an error. The non-linearity might come from the previously discussed wall/edge effects, which depend slightly on the velocity. Yet, the kinetic constants obtained by both methods fall into the range reported in literature (Table S6), which differs widely from $5.0 \cdot 10^{-4}$ to $2.4 \cdot 10^{-1}$ cm/s due to dependence on the used method, electrode material and cleaning procedure as well as electrolyte composition.^[50–55]

For the Kouteck y-Levich analysis, the kinetic constants for the DEFCs were approximately half of the ones determined for the RRDE, while the kinetic constant of the RRDE was smallest using the method of Nicholson (Table 5). This is likely due to the distribution of the educt concentration on the DEFC that differs from the bulk concentration used in the calculation and the effect of convection on the educt concentration. We note that for slower reactions such as the oxygen reduction reaction, the specific activity did not differ significantly among an RDE and a different flow cell design with a single working electrode.^[56] Thus, the deviation in the kinetic constant among the devices is expected to vanish for slower kinetics, optimized geometry and flow velocity, which deserves an in-depth investigation that is beyond the scope of this report.

Conclusion

We investigated a DEFC configuration with equal electrode and channel width theoretically using analytic solutions and multi-physics simulations as well as experimentally. The more widely used RRDE served as a reference for the theoretical and experimental results of the DEFC. Both devices produced measurements of similar quality of the on the ferri-/ferrocyanide redox reaction on Pt electrodes in a potassium chloride electrolyte. The 3D simulations showed that the wall effect accounted for a reduction in current density of 4 to 10% where the largest impact was observed for the smallest channel ($d=2$ mm) and largest volume flow rate (10 mL/min) as expected. Consequently, the experiments were satisfactorily described by the analytic solutions for most of the investigated configurations. The measured limiting currents of the generator and collector electrodes matched that of the analytical solution and simulations for the RRDE and DEFCs with $w=(d=)$ 2.0 and 5.0 mm. The limiting generator current of the 7.5 mm DEFC could not be described by the analytical solution and neither generator nor collector currents agreed with the simulations; more research is needed to gain a full understanding, which is outside of the scope of this paper. The collection efficiencies of the DEFCs with $w=d=5.0$ mm and 7.5 mm were close to the analytically calculated values of 35.4% and nearly independent of the flow rate, while the DEFC with $w=d=2.0$ mm might have been operated in a regime where the collection efficiency depends on flow rate. The Koutecký-Levich and Nicholson methods yield kinetic constants in the same order of magnitude for the investigated channel widths and among the DEFC and RRDE. While the kinetic constants obtained by the Nicholson method are up to an order of magnitude larger as compared to the Koutecký-Levich method, the values obtained by both methods for both devices fall into the wide range of literature values. The observed trends suggest that narrower electrodes are beneficial for kinetic studies. We conclude that our DEFC with exchangeable electrodes has a convenient size to work with in spectroscopic investigations and can be described by the analytic solution for electrode widths ≤ 5 mm. Therefore, they are an attractive alternative to commercial RRDEs due to the flexibility to optimize the electrode materials and geometry for the desired experimental setup and reaction of interest.

Experimental Section

Material and chemicals

The electrolyte consisted of 2 mM potassium hexacyanoferrate from Merck (analytical grade $\geq 99\%$) and 0.1 M potassium chloride from Merck ($\geq 99.5\%$) in ≥ 18.2 M Ω Milli-Q[®] water. The electrolyte was purged with argon (5.0 AirLiquide Alphagaz) for longer than 45 minutes to remove all dissolved oxygen. All chemicals were used as received. During the measurements, the purging was continued by bubbling argon into the reservoir.

Rotating ring-disk setup

The experimental setup of the RRDE was composed of a custom-made cylindrical PTFE cell, a RRDE-3A rotator (ALS Japan Co Ltd.), a saturated calomel electrode (RE-2B, ALS Japan Co Ltd.) and a platinum counter electrode, both radially arranged around the RRDE at a distance of 17 mm. The RRDE (ALS Japan Co Ltd.) consisted of a 4 mm diameter platinum disk ($A=0.126$ cm²) as generating electrode and a concentric platinum ring with an inner diameter of 5 mm and an outer diameter of 7 mm as detection electrode, separated by a PTFE spacer. The disk and ring electrodes were separately polished with Al₂O₃ using 3 μ m and 0.04 μ m polishing slurries and cleaned in isopropanol, before being assembled. During the experiment the rotator was set to various rotation speeds (100, 200, 300, 400 and 500 rpm).

Flow cell setup

The cell parts of the DEFC were constructed out of polyoxymethylene (POM) due to its mechanical stability. All cell parts with contact to the electrolyte were cleaned by rinsing first with isopropanol, then with ≥ 18.2 M Ω Milli-Q[®] water, subsequently sonicated in ultrapure water for at least five minutes and air dried afterwards. The platinum electrodes (99.95% purity) had a size of 10 \times 5 \times 1 mm (length, width, thickness). They were polished using 3 μ m and 0.04 μ m polishing slurry made of Al₂O₃, cleaned with ultrapure water and isopropanol by sonication. The electrodes were then placed into the holder and wires were laid on the back of the electrodes for electrical connection. To tighten the system, Parafilm[®] was placed on top of the wire and electrodes and a PTFE block pressed the assembly together. The glassy carbon counter electrode was cleaned separately the same way as the Pt-electrodes and placed in the holder on top of the working electrodes. The saturated calomel electrode (SCE; RE-2BE ALS Japan Co Ltd.) was placed upstream of the working electrodes. Finally, the assembled cell was purged multiple times with argon to remove the oxygen in the system and the electrolyte was drawn into the channel. The flow in the channel was controlled using a LA100 syringe pump from HLL Landgraf Laborsysteme with a 50 mL Omnifix[®] syringe from B|Braun. The electrolyte was thereby drawn from a container with a constant argon flow and small overpressure through the cell into the syringe with flowrates ranging from 0.5 to 6 mL/min. The small overpressure was applied to avoid oxygen from entering the system. To build up and check that the cell was under a small overpressure the container had an extra outlet to an additional container with Milli-Q[®] water. The overpressure was guaranteed, as long as argon bubbles could be observed in the extra container.

Electrochemical measurements

For the electrochemical measurements, two Gamry instrument interfaces 1010 were used in bipotentiostat mode. The potentiostats were calibrated to correct for possible current offsets and cable capacitance. The resistance of the working electrodes was determined using impedance spectroscopy (1 MHz to 1 Hz) before the measurements and afterwards to detect possible problems with connections and to correct for the potential drop. The generator electrode was then cycled three times between 0.55 V vs. SCE and -0.3 V vs. SCE with a scan rate of 10 mV/s. The collector electrode was held at a constant potential of 0.55 V vs. SCE for the entire measurement. All electrochemical data were analyzed using a custom python script. Impedance correction by iR-subtraction was applied to all measurements. Additionally, a linear baseline of the collector electrode was subtracted from the data to correct for non-faradic and other background currents (Figure S18a,b). The generator current was corrected by subtracting the linear function fitted

to the data before the onset of the reduction (Figure S18c,d). The limiting currents were obtained from the anodic scan for potentials with constant current. For most measurements this was the case between 0 and -0.2 V vs. SCE. In the case of slower flow rates, the potential windows had to be shifted to lower values due to the residue of the reduction peak. However, in no case was a limit lower than -0.28 V vs. SCE chosen to avoid possible artefacts from changing the scan direction.

Simulations

Steady-state simulations were performed with COMSOL Multiphysics® using PARDISO general solver using the Fluid Flow, Electrochemistry and Chemical species transport modules. Relative tolerance of 0.001 was applied as the convergence criterion. 3D fluid dynamic simulations were first performed based on the geometry of our 5 mm experimental DEFC (further parameters in Table 1, Table S7). Because our flow cell has a sufficient entrance length to develop laminar flow before reaching the electrodes (Figure S2), constant velocity field shown in Figure 3a was applied over the electrodes in the following mass transport simulation. With the simulated velocity field, the mass transport equation (Eq. 4) was numerically solved in 3D models with the limiting boundary conditions of $[\text{Fe}(\text{CN})_6^{3-}] = 0$ on the generator and $[\text{Fe}(\text{CN})_6^{4-}] = 0$ on the collector electrode. For a fair comparison between the limiting currents in 2D and 3D simulations, comparable mesh sizes were introduced. The mesh size close to the electrode was obtained from a previous report^[1] as shown in Figure S20. Furthermore, the mesh size was optimized using 2D simulations (Figure S19) before they were used in the 3D simulations (Figure S19). This resulted in a large number of meshes in the 3D model; the channel was then partitioned into a series of boxes of 1 mm length, in order to make the calculations more manageable (Figure S20). The concentration profile at the outlet of the previous box was used as the boundary condition at the inlet of the succeeding box. We validated this approach in a 2D model (i.e. without walls), where the same limiting currents and collection efficiency were obtained for the separated channel and single full channel (results are not shown). Local current density is obtained from the flux at the electrode by eq. 2. The simulated limiting current densities on the generator and the collector were further introduced to 3D model to determine the local current density on the counter electrode, which then determines the flux of products from the counter electrode.

$$\nabla \cdot \vec{j}_i = 0 \quad (12)$$

$$\vec{j}_i = -\sigma \nabla \phi_i \quad (13)$$

where \vec{j}_i , σ and ϕ_i represent the ionic current vector, electrolyte conductivity, and electrolyte potential, respectively. Local current density at the electrode surface (j_s) is described by

$$\vec{n} \cdot \vec{j}_i = j_s \quad (14)$$

where \vec{n} denotes the normal vector to the boundary. The electrode was assumed to be highly conductive (i.e., no Ohmic loss). The potential of the counter electrode (ϕ_s) was set to 0 V. At the counter electrode surface, the following Butler-Volmer equation was applied

$$j_s = j_0 \left\{ \exp\left(\frac{\alpha_a F \eta}{RT}\right) - \exp\left(\frac{-\alpha_c F \eta}{RT}\right) \right\}, \quad (15)$$

in which j_0 , α_a , and α_c are the exchange current density, anodic and cathodic transfer coefficient, respectively. The overpotential (η) is described as follow.

$$\eta = \phi_s - \phi_i - E_{eq} \quad (16)$$

E_{eq} is the equilibrium potential. Since the reduction current on the generator is larger than the oxidation current on the collector, an additional anodic reaction takes place on the counter electrode to account for charge balance. This reaction is assumed to be the oxygen evolution reaction. The simulated local current density on the counter electrode determines the boundary condition for the flux of O_2 .

$$\frac{j_s}{nF} = \vec{n} \cdot \vec{J} \quad (17)$$

where \vec{J} is the flux vector. For simplicity, we ignored any concentration overpotentials due to pH gradient and assumed O_2 remains in the electrolyte as dissolved gases (i.e., no bubbles). We confirmed that these simplifications do not affect the limiting currents at the generator and collector, which are the main focus of this study.

Supporting information

Brief theory of mass transport on rotating ring-disk electrodes, additional simulations and experimental data. No additional references were cited in the supporting information.

Acknowledgements

This work received funding from the Deutsche Forschungsgemeinschaft (DFG, German Research Foundation) – 397636017 and under Germany's Excellence Strategy – EXC 2008/1 (UniSysCat) – 390540038 as well as from the German Helmholtz Association – Excellence Network – ExNet-0024-Phase2-3. The simulation work was also carried out with the support of the Helmholtz Energy Materials Foundry (HEMF), a large-scale distributed research infrastructure founded by the German Helmholtz Association. We like to thank Prof. Gunther Wittstock and Joaquin Morales-Santelices for helpful discussions. Open Access funding enabled and organized by Projekt DEAL.

Conflict of Interests

The authors declare no conflict of interest.

Data Availability Statement

The data that support the findings of this study are openly available in Zenodo at <https://doi.org/10.5281/zenodo.7751674>, reference number 7751674. A former version of this manuscript is deposited as preprint at: <https://chemrxiv.org/engage/chem->

rxiv/article-details/60c75283ee301c509cc7ac12 and <https://arxiv.org/abs/2012.00070>.

Keywords: analytic electrochemistry · flow cells · rotating-ring disk electrodes · Multiphysics simulations · in situ experiments

- [1] R. G. Compton, G. M. Stearn, P. R. Unwin, A. J. Barwise, *J. Appl. Electrochem.* **1988**, *18*, 657–665.
- [2] H. Wang, E. Rus, H. D. Abruña, *Anal. Chem.* **2010**, *82*, 4319–4324.
- [3] J. Scholz, M. Risch, K. A. Stoerzinger, G. Wartner, Y. Shao-Horn, C. Jooss, *J. Phys. Chem. C* **2016**, *120*, 27746–27756.
- [4] U. A. Paulus, T. J. Schmidt, H. A. Gasteiger, R. J. Behm, *J. Electroanal. Chem.* **2001**, *495*, 134–145.
- [5] J. G. Vos, M. T. M. Koper, *J. Electroanal. Chem.* **2018**, *819*, 260–268.
- [6] R. Morasch, D. G. Kwabi, M. Tulodziecki, M. Risch, S. Zhang, Y. Shao-Horn, *ACS Appl. Mater. Interfaces* **2017**, *9*, 4374–4381.
- [7] J. G. Vos, M. T. M. Koper, *J. Electroanal. Chem.* **2019**, *850*, 113363.
- [8] I. S. Filimonenkov, S. Y. Istomin, E. V. Antipov, G. A. Tsirlina, E. R. Savinova, *Electrochim. Acta* **2018**, *286*, 304–312.
- [9] S. Vesztergom, N. Barankai, N. Kovács, M. Ujvári, P. Broekmann, H. Siegenthaler, G. G. Láng, *Electrochem. Commun.* **2016**, *68*, 54–58.
- [10] A. R. Mount, *Encycl. Electrochem.* (Eds.: P. R. Unwin, A. J. Bard, M. Stratman), Wiley-VCH Verlag **2003**, p. 134.
- [11] M. Baumung, F. Schönwald, T. Erichsen, C. A. Volkert, M. Risch, *Sustain. Energy Fuels* **2019**, *3*, 2218–2226.
- [12] M. Baumung, L. Kollenbach, L. Xi, M. Risch, *ChemPhysChem* **2019**, *20*, 2981–2988.
- [13] E. O. Barnes, G. E. M. Lewis, S. E. C. Dale, F. Marken, R. G. Compton, P. C. B. Page, J. del Campo, R. Mas, F. X. Muoz, R. G. Compton, *Analyst* **2012**, *137*, 1068.
- [14] V. Hermann, D. Dutriat, S. Müller, C. Comninellis, *Electrochim. Acta* **2000**, *46*, 365–372.
- [15] N. Heller-Ling, G. Poillerat, J. F. Koenig, J. L. Gautier, P. Chartier, *Electrochim. Acta* **1994**, *39*, 1669–1674.
- [16] E. Ríos, H. Reyes, J. Ortiz, J. L. Gautier, *Electrochim. Acta* **2005**, *50*, 2705–2711.
- [17] J. A. Cooper, R. G. Compton, *Electroanalysis* **1998**, *10*, 141–155.
- [18] G. W. Schieffer, W. J. Blaedel, *Anal. Chem.* **1977**, *49*, 49–53.
- [19] R. G. Compton, B. A. Coles, A. C. Fisher, *J. Phys. Chem.* **1994**, *98*, 2441–2445.
- [20] R. G. Compton, B. A. Coles, J. J. Gooding, A. C. Fisher, T. I. Cox, *J. Phys. Chem.* **1994**, *98*, 2446–2451.
- [21] K. Yunus, A. C. Fisher, *Electroanalysis* **2003**, *15*, 1782–1786.
- [22] W. J. Aixill, A. C. Fisher, Q. Fulian, *J. Phys. Chem.* **1996**, *100*, 14067–14073.
- [23] S. M. Matthews, G. Q. Du, A. C. Fisher, *J. Solid State Electrochem.* **2006**, *10*, 817–825.
- [24] C. Amatore, N. Da Mota, C. Sella, L. Thouin, *Anal. Chem.* **2007**, *79*, 8502–8510.
- [25] C. Amatore, N. Da Mota, C. Lemmer, C. Pebay, C. Sella, L. Thouin, *Anal. Chem.* **2008**, *80*, 9483–9490.
- [26] C. Amatore, N. Da Mota, C. Sella, L. Thouin, *Anal. Chem.* **2010**, *82*, 2434–2440.
- [27] J. L. Bott-Neto, M. V. F. Rodrigues, M. C. Silva, E. B. Carneiro-Neto, G. Wosiak, J. C. Mauricio, E. C. Pereira, S. J. A. Figueroa, P. S. Fernández, *ChemElectroChem* **2020**, *7*, 4306–4313.
- [28] K. Y. Tam, R. L. Wang, C. W. Lee, R. G. Compton, *Electroanalysis* **1997**, *9*, 219–224.
- [29] R. L. Wang, K. Y. Tam, F. Marken, R. G. Compton, *Electroanalysis* **1997**, *9*, 284–287.
- [30] M. Risch, K. A. Stoerzinger, B. Han, T. Z. Regier, D. Peak, S. Y. Sayed, C. Wei, Z. J. Xu, Y. Shao-Horn, *J. Phys. Chem. C* **2017**, *121*, 17682–17692.
- [31] T. Binninger, E. Fabbri, A. Patru, M. Garganourakis, J. Han, D. F. Abbott, O. Sereida, R. Kötz, A. Menzel, M. Nachttegaal, T. J. Schmidt, *J. Electrochem. Soc.* **2016**, *163*, H906–H912.
- [32] S. J. Ashton, *Design, Construction and Research Application of a Differential Electrochemical Mass Spectrometer (DEMS)*, Springer Berlin Heidelberg, Berlin, Heidelberg, Heidelberg **2012**.
- [33] W. G. Cochran, *Math. Proc. Cambridge Philos. Soc.* **1934**, *30*, 365–375.
- [34] A. J. Bard, L. R. Faulkner, *Electrochemical Methods: Fundamentals and Applications*, Wiley **2001**.
- [35] R. G. Compton, C. E. Banks, *Understanding Voltammetry, 2nd Edition*, Imperial College Press **2010**.
- [36] M. Risch, K. A. Stoerzinger, T. Z. Regier, D. Peak, S. Y. Sayed, Y. Shao-Horn, *J. Phys. Chem. C* **2015**, *119*, 18903–18910.
- [37] S. Moldoveanu, G. S. Handler, J. L. Anderson, *J. Electroanal. Chem.* **1984**, *179*, 119–130.
- [38] R. G. Compton, P. R. Unwin, *J. Electroanal. Chem. Interfacial Electrochem.* **1986**, *205*, 1–20.
- [39] S. G. Weber, W. C. Purdy, *Anal. Chim. Acta* **1978**, *100*, 531–544.
- [40] N. P. C. Stevens, A. C. Fisher, *J. Phys. Chem. B* **1997**, *101*, 8259–8263.
- [41] K. Aoki, K. Tokuda, H. Matsuda, *J. Electroanal. Chem.* **1987**, *217*, 33–47.
- [42] R. G. Compton, G. M. Stearn, *J. Chem. Soc. Faraday Trans. 1* **1988**, *84*, 4359–4367.
- [43] C. Amatore, O. V. Klymenko, I. Svir, *ChemPhysChem* **2006**, *7*, 482–487.
- [44] N. Kulyk, S. Cherevko, M. Auinger, C. Laska, K. J. J. Mayrhofer, *J. Electrochem. Soc.* **2015**, *162*, H860–H866.
- [45] S. A. Tschupp, S. E. Temmel, N. P. Salguero, J. Herranz, T. J. Schmidt, *J. Electrochem. Soc.* **2017**, *164*, E3448–E3456.
- [46] R. G. Compton, J. J. Gooding, A. Sokirko, *J. Appl. Electrochem.* **1996**, *26*, 463–469.
- [47] E. P. Schoch, W. A. Felsing, *J. Am. Chem. Soc.* **1916**, *38*, 1928–1947.
- [48] D. A. Scherson, Y. V. Tolmachev, Z. Wang, J. Wang, A. Palencsar, *Electrochem. Solid-State Lett.* **2008**, *11*, F1.
- [49] R. S. Nicholson, *Anal. Chem.* **1965**, *37*, 1354–1355.
- [50] P. H. Daum, C. G. Enke, *Anal. Chem.* **1969**, *41*, 653–656.
- [51] D. H. Angell, T. Dickinson, *J. Electroanal. Chem. Interfacial Electrochem.* **1972**, *35*, 55–72.
- [52] C. M. Pharr, P. R. Griffiths, *Anal. Chem.* **1997**, *69*, 4673–4679.
- [53] J. Jordan, *Anal. Chem.* **1955**, *27*, 1708–1711.
- [54] R. V. Bucur, A. Bartes, *Electrochim. Acta* **1979**, *24*, 173–178.
- [55] J. E. B. Randles, K. W. Somerton, *Trans. Faraday Soc.* **1952**, *48*, 937–950.
- [56] S. E. Temmel, S. A. Tschupp, T. J. Schmidt, *Rev. Sci. Instrum.* **2016**, *87*, 045115.

Manuscript received: March 20, 2023

Revised manuscript received: May 5, 2023

Version of record online: June 6, 2023